J. Fluid Mech. (1998), *vol.* 369, *pp.* 175–190. Printed in the United Kingdom

© 1998 Cambridge University Press

Instabilities of the undertow

By LI LI[1] AND ROBERT A. DALRYMPLE[1]

[1]Center for Applied Coastal Research, Department of Civil and Environmental Engineering, University of Delaware, Newark, DE 19716, USA

(Received 20 June 1997 and in revised form 10 March 1998)

The steady undertow created by waves breaking at a beach and slowly flowing offshore can become unstable and create a train of submerged offshore migrating vortices with shorter length scales and longer time scales than the incident waves, as shown by Matsunaga, Takehara & Awaya (1988, 1994). These vortices rotate about horizontal axes parallel to the shoreline. Our larger-scale laboratory experiments show that an additional layer of vortices can exist over the water depth, with vortices near the water surface rotating in the same direction as the wave-induced water particle trajectories, while those located at about mid-depth rotate in the opposite direction.

A theoretical and numerical analysis shows that these vortices are due to instabilities of the undertow. Far offshore of the surf zone, the vortex trains decay because the velocity profile for the undertow becomes linear over depth, hence neutrally stable to any disturbances.

1. Introduction

Waves breaking at the shoreline usually drive a nearshore circulation system, consisting of longshore, rip, and cross-shore currents. The latter currents are the mass transport of water to the shoreline (Stokes drift) and the so-called undertow, which returns the water to the offshore. This undertow also plays a critical role in the nearshore mixing (Svendsen & Putrevu 1992), particularly at the breaker line.

A number of studies on the velocities inside the surf zone have been carried out through field and laboratory measurements to reveal the cross-shore circulation system. Nadaoka & Kondoh (1982) made detailed laboratory measurements of the undertow inside and outside the surf zone. They found that outside the surf zone the undertow velocity profile has little curvature; it typically has a small seaward directed velocity at the bed and a larger seaward oriented velocity at the trough level. Putrevu & Svendsen (1993) applied a theoretical analysis to undertow structure outside the surf zone and obtained a linear mean velocity profile outside the boundary layer. These features also appear in the laboratory measurements of the velocities under regular waves spilling on a 1:35 impermeable slope by Cox, Kobayashi & Okayasu (1995).

Experiments on mass transport outside the surf zone by Bagnold (1947), using two-dimensional surface waves propagating over a horizontal smooth bed, showed a strong shoreward drift current along the bed, and a seaward one induced under the water surface. Longuet-Higgins (1953) explained this theoretically by taking into account the existence of a Stokes layer and viscosity. Dore (1970) found that the presence of surface viscosity greatly enhanced the drift velocity of short waves for interfacial waves on a clean interface. Then he pointed out that the air boundary layer

https://doi.org/10.1017/S0022112098001694 Published online by Cambridge University Press

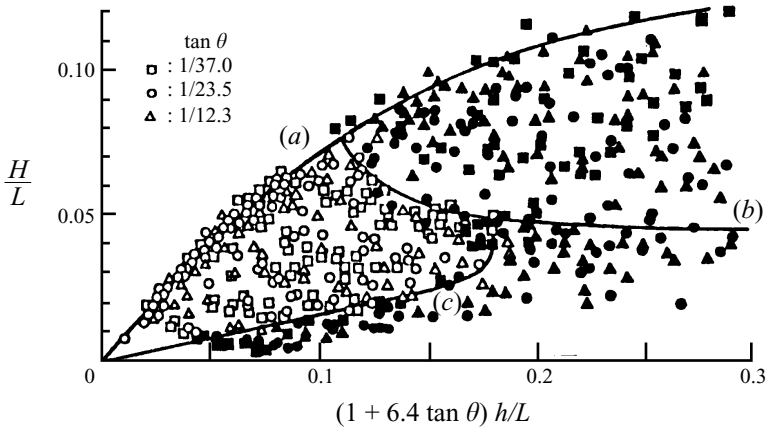


FIGURE 1. Formation regions of offshore vortices from Matsunaga *et al* (1994): open symbols, formation of offshore vortex; solid symbols, non-formation. Lines (*a*) and (*b*) indicate the limit of wave steepness and $H_0/L_0 = 4.2 \times 10^{-2}$, respectively. Line (*c*) is the offshore border of vortex formation.

greatly affects surface waves with long wavelength. He further concluded that the mean Eulerian velocity near the surface directed in the onshore direction far exceeded the magnitude of the Stokes drift. Craik (1982) later reached a similar conclusion.

Matsunaga, Takehara & Awaya (1988, 1994) discovered in a small wave tank (12 m long, 0.4 m deep, 0.15 m wide and equipped with a sloping planar bed) that the mean flow in the cross-shore direction just offshore of the breaker line was subject to a remarkable instability. The mean flow in the seaward direction became unstable and created a single layer of very large (order of the wave height) eddies slowly rotating about a horizontal axis parallel to the shoreline. These eddies rotated in an opposite sense to the trajectories of the wave-induced water particle motion. They called these eddies the offshore vortex train. As the vortices migrated offshore into greater depths, they decayed rapidly. This rotational motion contradicts the usual assumptions of irrotational wave motion. These authors also developed a number of empirical relationships describing the vortices. For example, they showed that the vortices occurred regardless of the breaker type and that there was a relationship between the relative water depth, the wave steepness, and the occurrence of the eddies. Figure 1 shows their unified plot of the vortices formation diagram, with $\tan\theta$ denoting the beach slope, and the open symbols showing when vortices formed in their experiments and the closed symbols denoting no eddy formation. For their modified relative water depths ($(1 + 6.4\tan\theta)h/L$, where h was the still water depth and L was the wavelength) exceeding 0.18, no vortices were observed. Also, there was a threshold wave steepness below which no eddies occur. Matsunaga *et al.* (1988, 1994) indicate that a shear instability may be responsible for the offshore vortex train, but provide no theoretical analysis.

This paper examines the offshore vortex train through both experimental and numerical approaches. First, in § 2, we describe the experiments carried out to verify the results of Matsunaga *et al.* in a larger wave tank. Measurements of the wave-averaged Eulerian velocity profile outside the surf zone were made using a SONTEK three-dimensional acoustic Doppler velocimeter (ADV). Some properties of the offshore vortex train were investigated using aniline dye as well. Then, in § 3, a linear model

https://doi.org/10.1017/S0022112098001694 Published online by Cambridge University Press

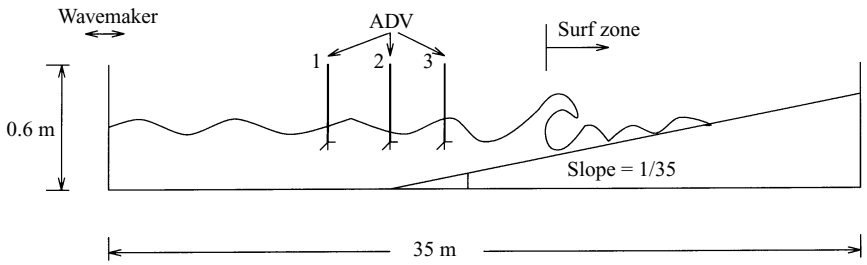


FIGURE 2. Schematic of experiment set-up.

Test	ADV	Wave period (s)	Water depth (m)	L (m)	h/L	H/L	Ursell number	$(1+6.4\tan\theta)h/L$	Existence of vortices
1	2	2.0	0.303	3.276	0.0925	0.0272	0.4357	0.1094	Yes
2	1	2.0	0.310	3.330	0.0946	0.0267	0.4000	0.1119	Yes
3	3	2.0	0.275	3.132	0.0878	0.0301	0.5652	0.1039	Yes
4	1	2.0	0.313	3.323	0.0942	0.0285	0.4319	0.1114	Yes
5	3	1.4	0.270	2.067	0.1306	0.0676	0.3844	0.1545	Yes
6	1	1.4	0.381	2.353	0.1619	0.0594	0.1773	0.1915	Yes
7	3	1.1	0.310	1.507	0.2057	0.0970	0.1413	0.2433	No
8	1	1.1	0.418	1.620	0.2580	0.0900	0.0664	0.3052	No

TABLE 1. List of experiments.

is used to investigate these vortex trains based on a shear instability of the mean offshore flow.

2. Experimental study

2.1. *Experiment set-up*

Figure 2 shows a schematic of the experimental set-up. Our experimental wave tank (35 m long, 0.6 m deep and 0.6 m wide) is 3 times longer, 4 times wider and 1.5 times deeper than the wave tank used by Matsunaga *et al.* (1988, 1994). It had a constant depth section at the wavemaker and a sloping planar bed with 1:35 slope at the other end. A piston wavemaker was used to generate the two-dimensional periodic surface waves. As shown in figure 2, three ADVs were used at three different locations: one is in the area with constant depth at least 10 m away from wavemaker, one is in the area where the sloping bed starts, the last one is in the area with sloping bed at least 2 m away from the breaking point.

The local wave height H and wave period T were measured using capacitance wave gauges. The local phase velocity C was calculated from the time lag of signals from two wave gauges that were located 20 cm apart in the constant depth section of the wave tank. The local wavelength L was then determined from the product of the celerity and wave period.

Eight tests, numbered 1–8, exploring the effect of varying local water depth h and wave frequencies on the offshore vortex train, were conducted as shown in table 1.

Based on the study of Matsunaga *et al.* (1994), tests 1–4 were designed to have the dimensionless wave height (H/L) and dimensionless water depth (h/L) combinations that would always generate vortices. Test 5 and test 6 were to study the cases where

https://doi.org/10.1017/S0022112098001694 Published online by Cambridge University Press



FIGURE 3. Dye pattern 150 wave periods after dye injection. The water wave propagates from left to right.

the occurrence of vortices varies. Test 7 and test 8 focused on the combinations that would lead to no vortices.

The vortex train induced offshore of the breaking point was observed by flow visualization. Granules of water-soluble aniline blue dye was used as a tracer. Typical flow patterns generated with a 2.0 s wave in a still water depth $h = 0.297$ m were photographed through the glass sidewall of the tank using a 35 mm camera. The direction of wave propagation was from left to right in all the photos presented below. The vortices were also videotaped to evaluate their characteristic quantities, e.g. the horizontal length scale of vortices, etc. These data were later used for comparison with the theoretical predictions.

2.2. *Experimental results*

Figures 3–5, taken at a fixed location, show the migration of the vortex system in the offshore direction (left) as reflected by the movement of the dye. The pictures were taken at 2 m away downstream from the injection point 5 s apart. It can be seen, particularly in figure 5, that there are two layers of vortices, one near the water surface (approximately 0.05 m below the water surface), with small vortices, and the other near the mid-depth (approximately 0.1 m below water surface), indicating the existence of two shear layers. Vortices near the water surface rotate in the opposite direction to vortices at mid-depth. The rotation direction of vortices near mid-depth was observed to be counter to the wave-induced water particle trajectories, as shown by Matsunaga *et al.* (1994), while the rotation direction of the upper layer of vortices has the opposite sense. These vortices rotate slowly with respect to water particle orbital motions, they migrate seaward slower than the undertow, they are embedded within the orbital wave motion, and there is very little dispersion of the dye by turbulence. The upper-layer vortices migrate at the same velocity as the lower-layer vortices, and have the same separation distance as those in the lower layer.

In each experiment, the offshore migration velocity of the vortex u_v was obtained by determining the time taken for a vortex to move a given distance. For test 2, the surface wave phase speed was $C = 1.33\,\mathrm{m\,s^{-1}}$, average vortex migration speed was $u_v = 0.0072\,\mathrm{m\,s^{-1}}$. The average time for a complete rotation of 360° of an eddy, T_v, was 21.5 s, about 10 times the surface wave period.

https://doi.org/10.1017/S0022112098001694 Published online by Cambridge University Press



FIGURE 4. Dye pattern 155 wave periods after dye injection.

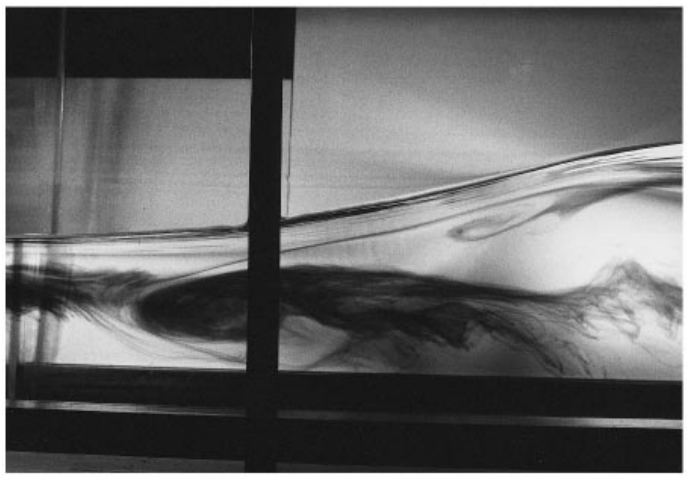


FIGURE 5. Dye pattern 160.9 wave periods after dye injection.

As we will show later numerically, the existence of one or two vortex layers is sensitive to the mean wave-induced velocity profile. Figure 6 shows the wave-averaged mean velocity profiles measured by the ADV for the eight experiments. The velocities were recorded through each ADV at a frequency of 50 Hz for a duration of 110 s. The wave-averaged profile results from assuming that the measured velocities consist of a steady wave-induced current component U, turbulent components u', w', the wave orbital wave motions u_w, w_w, and the longer-time-scale rotational components $\tilde{u}$, $\tilde{w}$ due to the vorticies. The plotted velocities were obtained by low passing the data to remove the wave-induced and the turbulent velocities and leaving the mean current and the longer-time-scale components that cannot be filtered. For example, the low-passing frequency used for tests 1 and 2 was 1.25 Hz. Rather than a straight-line distribution over the depth, the resulting velocity profiles are curved. Changes in the curvature of these profiles correspond to the presence of shear layers. It is seen from figure 6 that there are two points over water depth where the second derivative of

https://doi.org/10.1017/S0022112098001694 Published online by Cambridge University Press

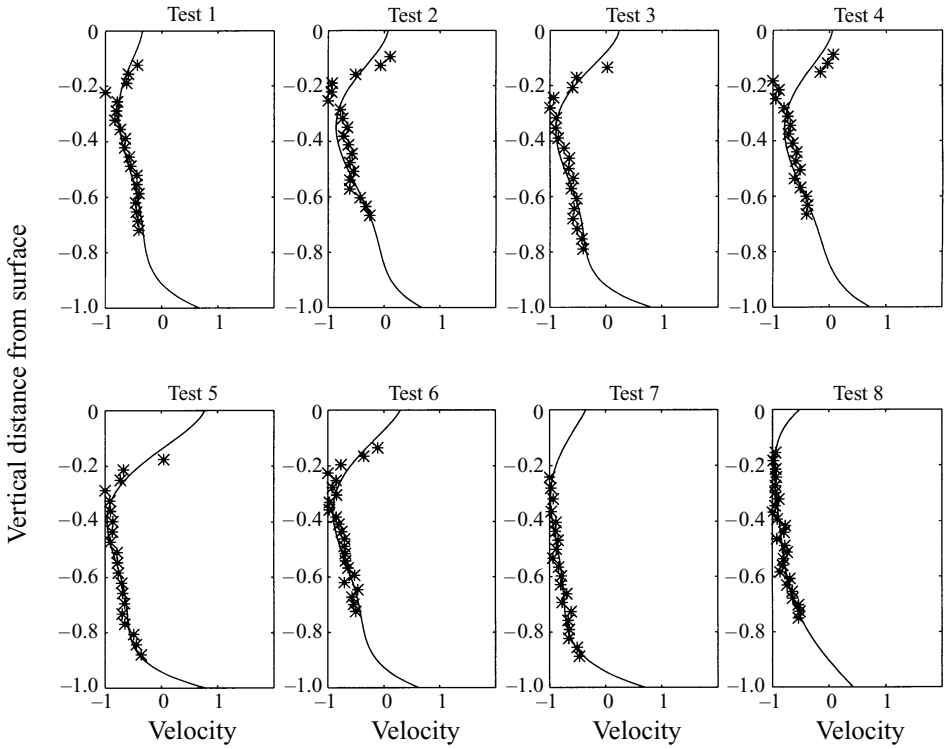


FIGURE 6. Undertow profile for each test versus non-dimensional depth: *, experiment data; solid line, the smoothed velocity profile used for the numerical study.

velocity (d^2U/dz^2) becomes zero, implying the existence of two shear layers. Tests 7 and 8 show little curvature, but the measurements capture the relevant shear layer.

The plotted velocity data do include the influence of the vorticies on the mean profile; however this contribution is small. The averaged product $\overline{u'w'}$ represents the turbulent contribution to the momentum transfer, whereas the $\overline{u_w w_w}$ and the $\overline{\tilde{u}\tilde{w}}$ represent the wave contribution and contribution of the vortices, respectively. The average $\overline{\tilde{u}\tilde{w}}/\overline{u_w w_w}$ is less than 10%, implying that the vortex contribution to the momentum transfer is insignificant compared to the wave contribution.

The smooth velocity profile was obtained by fitting a fifth-order polynomial to the measured wave-averaged data. Since measurements were not taken at the bottom or the surface, due to proximity effects and the difficulty of measuring within the wave trough region, consideration of these boundaries is merited to determine their influence on the final fitted profile. One option is to leave these points free and let the fitting find values there. However, due to the high order of the fitting polynomial, this could lead to unrealistic values at these end points. At the bottom, we can fix the velocity approximately to that of the theoretical value at the top of the boundary layer $U = \frac{3}{4}\sigma a^2 k \operatorname{cosech}^2(kh)$, Craik (1982), where a is surface wave amplitude, k is surface wavenumber, and $\sigma = 2\pi/T$. Numerical experiments show that this bottom boundary velocity has no real influence on the fitting and our subsequent instability calculation. At the mean surface, the theoretical boundary condition is $dU/dz = 2\sigma a^2 k^2 \coth^2(kh)$, Craik (1982). However, if the value of the surface velocity were arbitrarily changed by $\pm 20\%$, the calculated instability wavenumber would change at most 6%, leading us to argue that the results are not very sensitive to the surface value either.

https://doi.org/10.1017/S0022112098001694 Published online by Cambridge University Press

Table 1 also shows the Ursell number Ur for all eight tests. The Ursell number represents the ratio of wave nonlinearity to frequency dispersion. Table 1 shows that tests 1–6, in which vortices were observed, have higher Ursell numbers, while tests 7 and 8, in which no vortices were noticed, have much lower Ursell number. Thus the nonlinearity of the surface wave is important for the presence of vortices, as shown by Matsunaga *et al.* (line (*c*) in figure 1).

3. Theoretical study

3.1. *Theory*

The vortices are embedded in orbital wave motion, and are considered to be the instabilities of the mean flow with longer time scales and shorter length scales than the incident waves. The governing equations for the longer-time-scale motion can be obtained by averaging first over the turbulence time scale, and then over the period of the incident wave. Next, through a perturbation analysis, the governing equations for the mean flow are derived at the zeroth order, and the stability equations of the interaction between disturbances and mean flow are generated at the first order.

The flow offshore of the surf zone is usually divided vertically into three regions: the surface boundary layer region, the core region, and the bottom boundary layer region. The Navier–Stokes equations and continuity equation for a homogeneous and incompressible fluid are adopted for this analysis. The coordinate x is in the wave propagation direction, z is vertically upward from the origin located at the mean free surface. All variables are non-dimensional: x, z are normalized by the water depth (L_{ref}). U_{ref}, which is the maximum velocity of the undertow, is used to non-dimensionalize all fluid velocities. Time t is normalized by a transit time associated with the undertow (L_{ref}/U_{ref}). As is customary, pressure is measured in terms of ρU_{ref}^2. The relevant Reynolds number is $Re = U_{ref}L_{ref}/\nu \gg 1$ where ν denotes the kinematic viscosity.

To treat the turbulence time scale, we introduce the Reynolds decomposition variables: $u = \widehat{u} + u'$, $w = \widehat{w} + w'$ and $p = \widehat{p} + p'$, where $\widehat{\ }$ denotes ensemble average, and $\widehat{u'} = 0$, $\widehat{w'} = 0$ and $\widehat{p'} = 0$. The governing equations can be ensemble averaged over a short period of time to obtain the Reynolds–Navier–Stokes equations:

$$\frac{\partial \widehat{u}}{\partial t} + \widehat{u}\frac{\partial \widehat{u}}{\partial x} + \widehat{w}\frac{\partial \widehat{u}}{\partial z} = -\frac{\partial \widehat{p}}{\partial x} - \frac{\partial \widehat{u'^2}}{\partial x} - \frac{\partial \widehat{u'w'}}{\partial z} + \frac{1}{Re}\left(\frac{\partial^2 \widehat{u}}{\partial x^2} + \frac{\partial^2 \widehat{u}}{\partial z^2}\right), \tag{3.1}$$

$$\frac{\partial \widehat{w}}{\partial t} + \widehat{u}\frac{\partial \widehat{w}}{\partial x} + \widehat{w}\frac{\partial \widehat{w}}{\partial z} = -\frac{\partial \widehat{p}}{\partial z} - \frac{\partial \widehat{u'w'}}{\partial x} - \frac{\partial \widehat{w'^2}}{\partial z} + \frac{1}{Re}\left(\frac{\partial^2 \widehat{w}}{\partial x^2} + \frac{\partial^2 \widehat{w}}{\partial z^2}\right), \tag{3.2}$$

$$\frac{\partial \widehat{u}}{\partial x} + \frac{\partial \widehat{w}}{\partial z} = 0. \tag{3.3}$$

The boundary conditions at the free surface are that the tangential stress is zero

$$\frac{\partial \widehat{u}}{\partial z} + \frac{\partial \widehat{w}}{\partial x} = 0 \quad \text{at } z = 0, \tag{3.4}$$

and that the normal stress is zero

$$-P_a + 2\frac{1}{Re}\frac{\partial \widehat{w}}{\partial z} = 0 \quad \text{at } z = 0, \tag{3.5}$$

where P_a is the atmospheric pressure.

https://doi.org/10.1017/S0022112098001694 Published online by Cambridge University Press

The boundary conditions at the rigid bottom are

$$\widehat{u} = \widehat{w} = 0 \quad \text{at } z = -h. \tag{3.6}$$

The three correlation terms $-\widehat{u'^2}$, $-\widehat{u'w'}$ and $-\widehat{w'^2}$ are turbulent stresses.

For convenience, the $\widehat{\ }$ symbol for u and w is omitted in the following. Based on the results from the experiments, the vortex has a much longer time scale than the surface waves. Therefore, we can assume that the Reynolds-averaged velocities consist of a steady wave-induced current component $U(x,z)$, the wave orbital motions $u_w(x,z,t)$, $w_w(x,z,t)$, and a higher-order longer-time-scale perturbation component $\tilde{u}(x,z,t)$, $\tilde{w}(x,z,t)$:

$$u = U(x,z) + u_w(x,z,t) + \varepsilon\tilde{u}(x,z,t), \tag{3.7}$$

$$w = w_w(x,z,t) + \varepsilon\tilde{w}(x,z,t), \tag{3.8}$$

$$p = p(x,z) + \varepsilon\tilde{p}(x,z), \tag{3.9}$$

where ε is an arbitrary small constant which may be interpreted as a measure of the magnitude of the disturbance.

Gathering all the terms that do not depend on ε, the lowest-order governing equations for the wave-induced water particle velocities become

$$\frac{\partial u_w}{\partial t} + (U+u_w)\frac{\partial (U+u_w)}{\partial x} + w_w\frac{\partial (U+u_w)}{\partial z} = -\frac{\partial p}{\partial x} - \frac{\partial \widehat{u'^2}}{\partial x} - \frac{\partial \widehat{u'w'}}{\partial z} + \frac{1}{Re}\left(\frac{\partial^2 (U+u_w)}{\partial x^2} + \frac{\partial^2 (U+u_w)}{\partial z^2}\right), \tag{3.10}$$

$$\frac{\partial w_w}{\partial t} + (U+u_w)\frac{\partial w_w}{\partial x} + w_w\frac{\partial w_w}{\partial z} = -\frac{\partial p}{\partial z} - \frac{\partial \widehat{u'w'}}{\partial x} - \frac{\partial \widehat{w'^2}}{\partial z} + \frac{1}{Re}\left(\frac{\partial^2 w_w}{\partial x^2} + \frac{\partial^2 w_w}{\partial z^2}\right), \tag{3.11}$$

$$\frac{\partial (U+u_w)}{\partial x} + \frac{\partial w_w}{\partial z} = 0, \tag{3.12}$$

with boundary conditions

$$\frac{\partial U+u_w}{\partial z} + \frac{\partial w_w}{\partial x} = P_a + 2\frac{1}{Re}\frac{\partial w_w}{\partial z} = 0 \quad \text{at } z = 0, \tag{3.13}$$

$$U + u_w = w_w = 0 \quad \text{at } z = -h. \tag{3.14}$$

Averaging the above equations over the period of the incident wave gives the equation for the mean flow. If the turbulent stresses $-\widehat{u'^2}$, $-\widehat{u'w'}$ and $-\widehat{w'^2}$ are not considered (Craik 1982), a steady mean Eulerian velocity $U(z)$ satisfies

$$\frac{1}{Re}\frac{\mathrm{d}^2 U}{\mathrm{d}z^2} = \frac{\mathrm{d}}{\mathrm{d}z}(\overline{u_w w_w}) + \frac{\mathrm{d}p}{\mathrm{d}x}, \tag{3.15}$$

where $\overline{u_w w_w}$ denotes the time-averaged Reynolds stress τ_{xz} resulting from the linear wave field. For zero mass flux, Craik obtained the corresponding velocity distribution in the core region:

$$U(z) = \tfrac{1}{2}(\sigma/2\mu)^{1/2}\sigma a^2 k \coth^2(kh)(z + h + \tfrac{3}{4}d^{-1}(z^2 - h^2)). \tag{3.16}$$

This undertow profile, however, does not contain inflection points as seen in our experiments. Therefore, we will use the measured undertow profiles in our numerical calculations that follow.

https://doi.org/10.1017/S0022112098001694 Published online by Cambridge University Press

At order ε, we obtain equations for the longer-time-scale velocities $\tilde{u}$, $\tilde{w}$:

$$\frac{\partial \tilde{u}}{\partial t} + (U + u_w)\frac{\partial \tilde{u}}{\partial x} + \tilde{u}\frac{\partial (U + u_w)}{\partial x} + \tilde{w}\frac{\partial (U + u_w)}{\partial z} + w_w\frac{\partial \tilde{u}}{\partial z} = -\frac{\partial \tilde{p}}{\partial x} + \frac{1}{Re}\left(\frac{\partial^2 \tilde{u}}{\partial x^2} + \frac{\partial^2 \tilde{u}}{\partial z^2}\right), \quad (3.17)$$

$$\frac{\partial \tilde{w}}{\partial t} + (U + u_w)\frac{\partial \tilde{w}}{\partial x} + \tilde{u}\frac{\partial w_w}{\partial x} + \tilde{w}\frac{\partial w_w}{\partial z} + w_w\frac{\partial \tilde{w}}{\partial z} = -\frac{\partial \tilde{p}}{\partial z} + \frac{1}{Re}\left(\frac{\partial^2 \tilde{w}}{\partial x^2} + \frac{\partial^2 \tilde{w}}{\partial z^2}\right) \quad (3.18)$$

$$\frac{\partial \tilde{u}}{\partial x} + \frac{\partial \tilde{w}}{\partial z} = 0, \quad (3.19)$$

with boundary conditions

$$\frac{\partial \tilde{u}}{\partial z} + \frac{\partial \tilde{w}}{\partial x} = \frac{\partial \tilde{w}}{\partial z} = 0 \quad \text{at } z = 0, \quad (3.20)$$

$$\tilde{u} = \tilde{w} = 0 \quad \text{at } z = -h. \quad (3.21)$$

We also average (3.17)–(3.19) over a wave period. Because $\tilde{u}$ and $\tilde{w}$ have a long time scale, their time derivatives can be treated as constants over one wave period, and the average of the products are: $\overline{rs_w} = 0$, $\overline{rU} = rU$, for $r = \tilde{u}, \tilde{w}$ and $s = u, w$. The steady current component U is assumed not to be a function of x.

Then (3.17)–(3.19) become

$$\frac{\partial \tilde{u}}{\partial t} + U\frac{\partial \tilde{u}}{\partial x} + \tilde{w}\frac{\partial U}{\partial z} = -\frac{\partial \tilde{p}}{\partial x} + \frac{1}{Re}\left(\frac{\partial^2 \tilde{u}}{\partial x^2} + \frac{\partial^2 \tilde{u}}{\partial z^2}\right), \quad (3.22)$$

$$\frac{\partial \tilde{w}}{\partial t} + U\frac{\partial \tilde{w}}{\partial x} = -\frac{\partial \tilde{p}}{\partial z} + \frac{1}{Re}\left(\frac{\partial^2 \tilde{w}}{\partial x^2} + \frac{\partial^2 \tilde{w}}{\partial z^2}\right), \quad (3.23)$$

$$\frac{\partial \tilde{u}}{\partial x} + \frac{\partial \tilde{w}}{\partial z} = 0. \quad (3.24)$$

Let us introduce a stream function ψ representing the long-period perturbation, such that

$$\tilde{u} = \frac{\partial \psi}{\partial z}, \quad \tilde{w} = -\frac{\partial \psi}{\partial x}$$

and

$$\psi(x, z, t) = \phi(z)\mathrm{e}^{\mathrm{i}\alpha(x - ct)},$$

where α is a wavenumber and c is the wave phase speed. Substituting ψ into the above equations yields the Orr–Sommerfeld equation for ϕ:

$$\frac{1}{\mathrm{i}\alpha Re}(\mathrm{D}^2 - \alpha^2)^2\phi = (U - c)(\mathrm{D}^2 - \alpha^2)\phi - U''\phi, \quad (3.25)$$

where $\mathrm{D}\phi = \phi'$.

The boundary conditions associated with (3.25) are

$$\phi'' + \alpha^2\phi = \phi' = 0 \quad \text{at } z = 0, \quad (3.26)$$

$$\phi = \phi' = 0 \quad \text{at } z = -h. \quad (3.27)$$

The boundary condition at $z = 0$ indicates that normal and shear stress are zero at the free surface. At the bottom, the rigid boundary condition applies.

The Orr–Sommerfeld equation describes shear instabilities (e.g. Drazin & Reid

https://doi.org/10.1017/S0022112098001694 Published online by Cambridge University Press

1981). Solutions of this equation will be progressive waves with phase velocity equal to the real part of c, which is the speed with which the entire perturbation pattern moves in the off-shore direction. For those values of the wavenumber for which c has a negative imaginary component, the solution has an exponentially growing amplitude which indicates that the cross-shore velocity profile, $U(z)$, is unstable with respect to that particular mode. For the case of plane Poiseuille flow (Lin 1955), experiments and experience suggest that instability can be found only for large values of αRe. The minimum critical Reynolds number is 5300, based on the maximum velocity at the centre of the channel and its half-width.

This Sturm–Liouville problem is difficult to solve analytically for an arbitrary velocity distribution $U(z)$. Therefore, a numerical approach was used.

3.2. *Numerical formulation*

Equation (3.25) was solved by finite differences. Representing the z-axis as $z = j\Delta z$, $j = 1, 2, \ldots, N$, $U(z)$ as U_j and $\phi(z)$ as ϕ_j, we can represent (3.25) as

$$a1\phi_{j+2} + a2\phi_{j+1} + a3\phi_j + a4\phi_{j-1} + a5\phi_{j-2} = c(\phi_{j+1} - (2 + \Delta z^2\alpha^2)\phi_j + \phi_{j-1}), \quad j = 1, 2, \ldots, N, \tag{3.28}$$

where

$$a1 = -\frac{1}{\mathrm{i}\alpha Re\Delta z^2}, \quad a2 = \frac{4}{\mathrm{i}\alpha Re\Delta z^2} + \frac{2\alpha}{\mathrm{i}Re} + U_j,$$
$$a3 = -\frac{6}{\mathrm{i}\alpha Re\Delta z^2} - \frac{4\alpha}{\mathrm{i}Re} - \frac{\alpha^3\Delta z^2}{\mathrm{i}Re} - ((2 + \Delta z^2\alpha^2)U_j + (U_{j+1} - 2U_j + U_{j-1})),$$
$$a4 = \frac{4}{\mathrm{i}\alpha Re\Delta z^2} + \frac{2\alpha}{\mathrm{i}Re} + U_j, \quad a5 = -\frac{1}{\mathrm{i}\alpha Re\Delta z^2}.$$

The same procedure can be applied to the boundary conditions. Applying this equation to all the j points and the boundary conditions yields a matrix equation:

$$\boldsymbol{A}\boldsymbol{\phi} = c\boldsymbol{B}\boldsymbol{\phi}. \tag{3.29}$$

Here, $\boldsymbol{A}$ and $\boldsymbol{B}$ are $N \times N$ matrices and $\boldsymbol{\phi}$ is a vector of size N. For the prescribed boundary conditions, this equation can be solved only for certain values of c, i.e. the eigenvalues. These eigenvalues of the matrix equation are equivalent to eigenvalues of (3.25). For each value of the wavenumber α, (3.29) will yield N eigenvalues. Eigenvalues with an imaginary component are of particular interest because they yield exponentially growing waves.

In cases where more than one such unstable eigenvalue is present, it is assumed that the one with the largest imaginary component will dominate the instability of that wave number. This corresponds to the point of maximum αc_{im}. The growth rate αc_{im} as a function of the instability wavenumber is shown in figure 7 for the undertow velocity of test 1; a comparison with the experimental study will be shown in the next section. If, for a particular value of α, all the eigenvalues are real, this implies that the cross-shore current is stable to disturbances with the wavenumber α.

Using the undertow velocities U measured in our experiments (i.e. the fitted velocity profiles based on the experiment data as shown in figure 6) and the relevant Reynolds number $Re = U_{ref}L_{ref}/\nu$ for each case, the numerical approach was used to predict the vortices generated under flow conditions similar to the cases in the experimental study. The numerical predictions were then compared with the results measured in the experimental study. The comparisons and discussion are presented in the next section.

https://doi.org/10.1017/S0022112098001694 Published online by Cambridge University Press

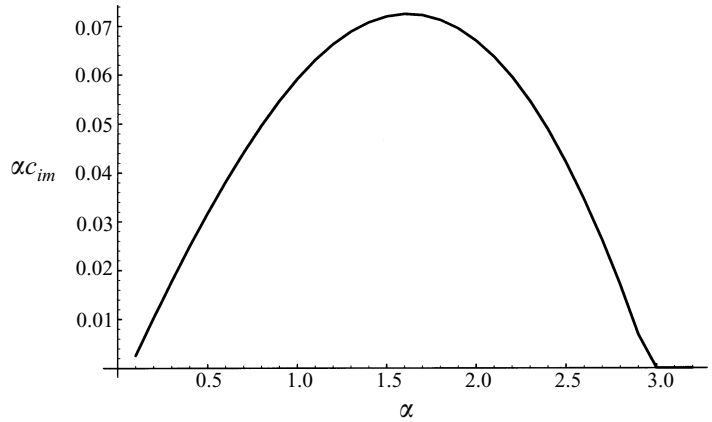


FIGURE 7. Frequency–wavenumber plots of the shear instability for the test 1, $T = 2.0\,\mathrm{s}$, $h = 0.303\,\mathrm{m}$.

Test	Experiment	Numerical result	Matsunaga *et al.* (1994)
1	0.386	0.391	0.437
2	0.275	0.350	0.463
3	0.330	0.331	0.358
4	0.279	0.347	0.431
5	0.195	0.261	0.157
6	0.316	0.370	0.252

TABLE 2. Comparison between the numerical solution and experimental results for the horizontal spacing between vortices (m).

	Near water surface		Near mid-depth	
Test	Experiment	Numerical result	Experiment	Numerical result
1	0.068	0.060	0.108	0.121
2	0.052	0.063	0.119	0.126
3	0.065	0.066	0.114	0.137
4	0.061	0.061	0.130	0.128
5	0.082	0.076	0.149	0.151
6	0.106	0.092	0.172	0.168

TABLE 3. Comparison between the numerical solution and experimental results for vertical distances of vortices from the mean water level (m).

4. Numerical results and discussion

While the instability occurs over a range of frequencies and wavenumber, there will be a single fastest growing wave that we can use to determine characteristic time and length scales. This corresponds to the point of maximum αc_{im} (figure 7). Using flow conditions similar to those in the experiments, horizontal length scales for the fastest growing instabilities calculated from the numerical model are shown in table 2 with the corresponding experimental results. The experimental and numerical results of the vertical distance of the instability from the mean water level are shown in table 3. It is seen that there is a good agreement between the experiment and numerical model. Tests 7 and 8 are not shown because, for any value of α, all

https://doi.org/10.1017/S0022112098001694 Published online by Cambridge University Press

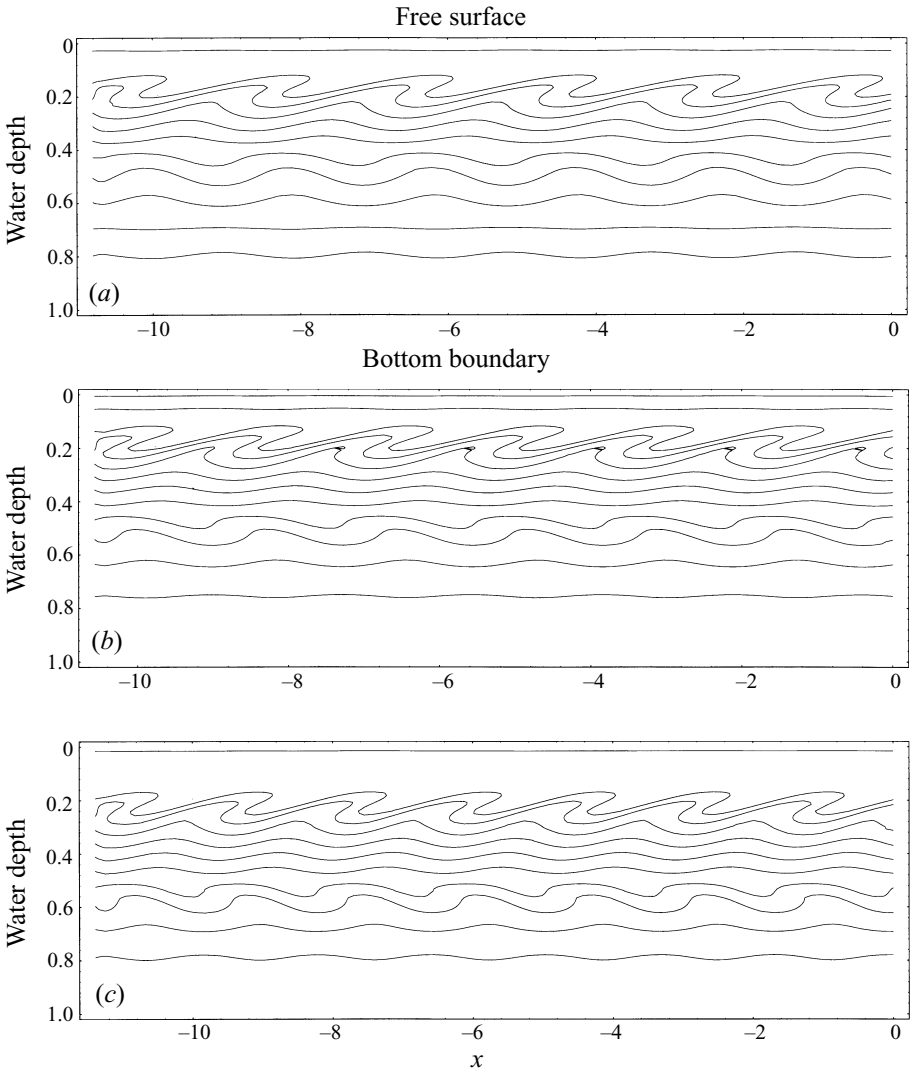


FIGURE 8(*a–c*). For caption see facing page.

the eigenvalues are real, which means that the undertow profile is neutrally stable. Clearly, the linear perturbation model can predict the position and length scale of the vortices.

Knowing the wavenumber of the unstable mode α, its speed of propagation c and ϕ, we can now calculate the spatial structure of the wave motions. Figure 8 shows the calculated total stream function for one surface wave wavelength using the undertow velocity profile and water depth for each experiment. The streamlines are obtained by summing the mean velocity and the unstable wave mode. Note that these figures show the linear solution for the unstable wave mode and therefore do not show the progression to the fully developed eddies seen in the experiments. Figure 9 shows the spatial patterns of the streamlines for a quarter surface wave and the associated velocities. Vortices near the water surface rotate in the opposite direction to vortices at mid-depth. For example, for the surface

https://doi.org/10.1017/S0022112098001694 Published online by Cambridge University Press

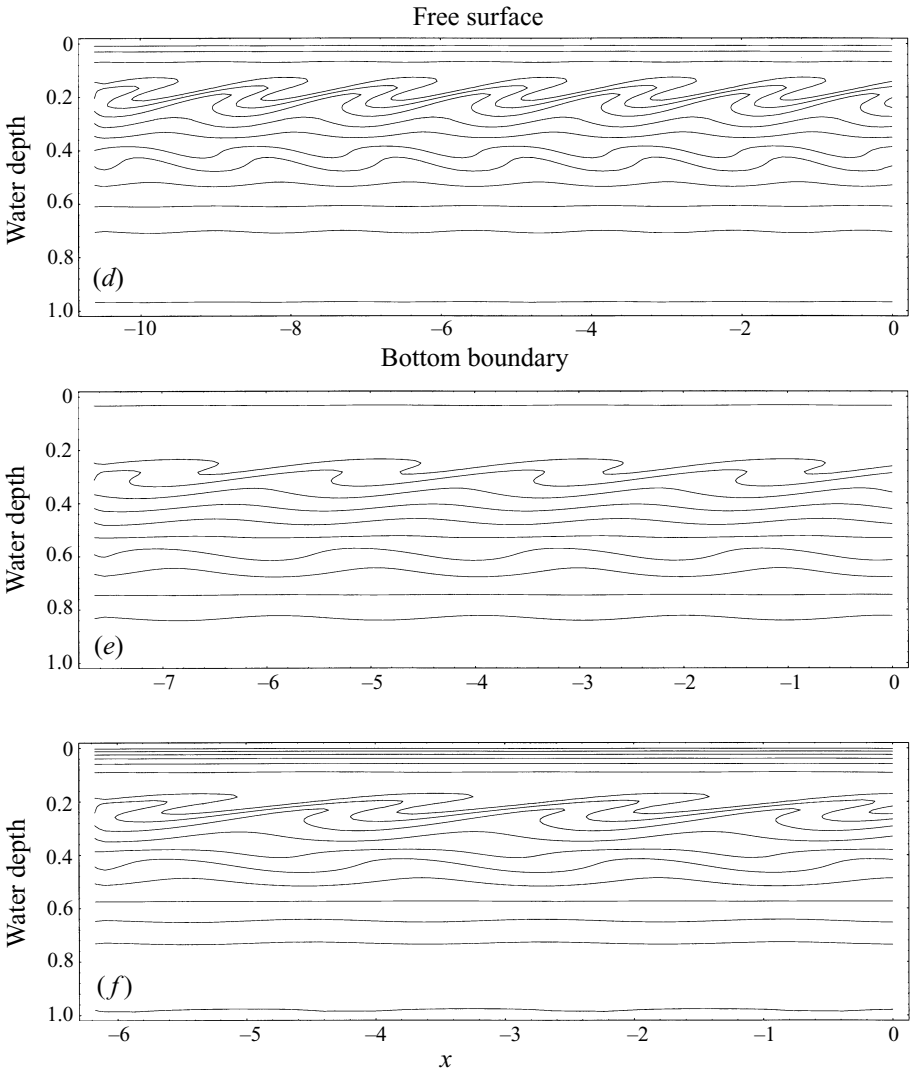


FIGURE 8. Stream function pattern of the instability over one surface wavelength, The surface wave propagates to the left: (*a*) test 1, (*b*) test 2, (*c*) test 3, (*d*) test 4, (*e*) test 5, (*f*) test 6.

wave propagating to the right, the rotation direction of vortices near mid-depth was counterclockwise, while the rotation direction of vortices near surface was clockwise. The unstable wave progresses in the offshore direction at both levels, similar to our laboratory observations. It is also shown that the unstable wavelength is much shorter than the surface wavelength. The two vortex layers shown in figure 8 indicate the existence of two shear layers, which is also confirmed in the experimental study.

Next, we examine the results of Matsunaga *et al.* (1988, 1994). The shape of a particular velocity profile based on their experiment, where $T = 1.06$ s, $\tan\theta = 1/23.5$ (figure 10) was obtained based on the deformation of dye lines shown in Matsunaga *et al* (1994). Using this, figure 11 gives the calculated spatial form of the stream function for one surface wave wavelength which shows a layer of eddies near mid-depth which

https://doi.org/10.1017/S0022112098001694 Published online by Cambridge University Press

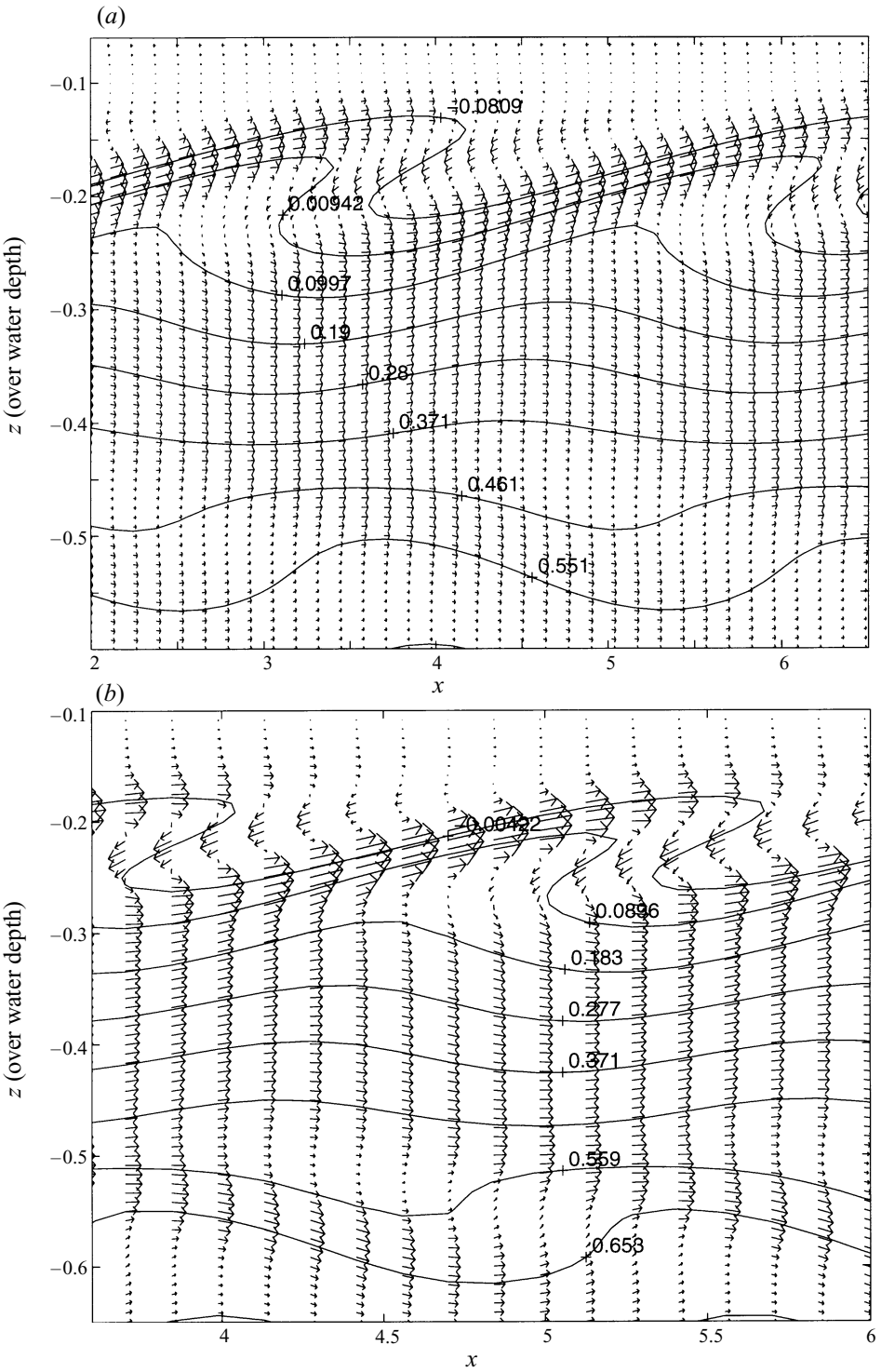


FIGURE 9. The spatial pattern of surface-wave-averaged total velocity field for (*a*) test 2 and (*b*) test 3, over a quarter surface wavelength. The surface wave propagates to the left.

https://doi.org/10.1017/S0022112098001694 Published online by Cambridge University Press

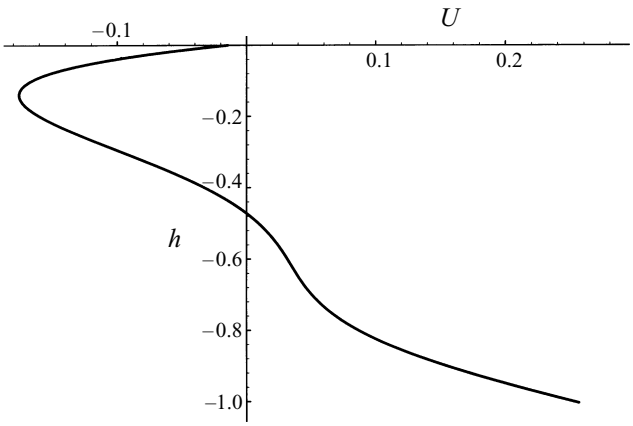


FIGURE 10. The velocity profile from Matsunaga *et al.* (1988, 1994), $T = 1.06$ s, $\tan\theta = 1/23.5$.

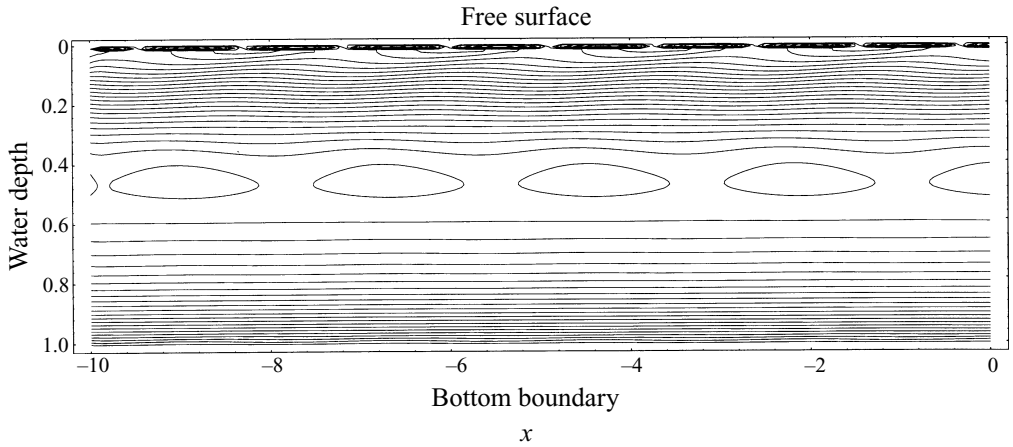


FIGURE 11. Stream function pattern of the instability over one surface wavelength from Matsunaga *et al.* (1988, 1994). The surface wave propagates to the right.

was observed by them. There are likely to be errors in our assumed velocity profile, having taken it from their figure. However, errors resulting in shifting the mean of the velocity profile around zero cause the eddies to appear either higher or lower in the water column, yet they always occur in a single layer.

5. Conclusions

Laboratory experiments and a numerical study show that the steady undertow outside the surf zone can be unstable to slow oscillations that are below water surface with shorter length scale and longer time scale than the incident surface waves. These instabilities lead to large eddies identified by Matsunaga *et al.* (1988, 1994) as the offshore vortex train.

In our experiment, two vortex layers exist over the water depth, because of the existence of two shear layers, rather than one as observed by Matsunaga *et al.* (1988, 1994). After reaching a particular offshore position the vortices decay because the

https://doi.org/10.1017/S0022112098001694 Published online by Cambridge University Press

velocity profile for undertow for that point becomes linear and neutrally stable to any disturbance.

The rotation of the eddies near the water surface is in the same direction as the orbital trajectories of the wave-induced water particle motions and in the opposite direction to the rotation of the eddies at mid-depth.

Using flow conditions similar to those in the experiments, horizontal length scales and vertical positions for the fastest growing instabilities calculated from the numerical model are shown with the corresponding experimental results. There is a good agreement between the experiment and numerical model. It may be concluded that the linear stability model can predict the occurrence of the vortices from the undertow profile.

The existence and the number of vortex layers are related to the mean velocity profile, which depends on the experimental conditions, such as water depth, wave height, wave nonlinearity and viscosity, etc. At present we do not have any quantitative explanation of when this will happen, since we do not have a theoretical mean velocity profile with shear layers.

REFERENCES

Bagnold, R. A. 1947 Sand movement by waves: some small scale experiments with sand of very low density. *J. Inst. Civil Engrs* **27**, 447–469.

Cox, D. T., Kobayashi, N. & Okayasu, A. 1995 Vertical variations of fluid velocities and shear stress in surf zones. *Proc. 24th Intl Coastal Engng Conf. ASCE* **1**, pp. 98–112.

Craik, A. D. D. 1982 The drift velocity of water waves. *J. Fluid Mech.* **116**, 187–205.

Dore, B. D. 1970 Mass transport in layered fluid systems. *J. Fluid Mech.* **40**, 113–126.

Drazin, P. G. & Reid, W. H. 1981 *Hydrodynamic Stability*. Cambridge University Press.

Lin, C. C. 1955 *The Theory of Hydrodynamic Stability*. Cambridge University Press.

Longuet-Higgins, M. S. 1953 Mass transport in water waves. *Phil. Trans. R. Soc. Lond.* A **245**, 535–581.

Matsunaga, N., Takehara, K. & Awaya, Y. 1988 Coherent eddies induced by breakers on a sloping bed. *Proc. 21st Intl Coastal Engng Conf. ASCE* pp. 234–245.

Matsunaga, N., Takehara, K. & Awaya, Y. 1994 The offshore vortex train. *J. Fluid Mech.* **276**, 113–124.

Nadaoka, K. & Kondoh, T. 1982 Laboratory measurements of velocity field structure in the surf zone. *Coastal Engng Japan* **25**, 125–145.

Putrevu, U. & Svendsen, I. A. 1993 Vertical structure of the undertow outside the surf zone. *J. Geophys. Res.* **98**, 22707–22716.

Svendsen, I. A. & Putrevu, U. 1992 A mixing mechanism in the nearshore region. *Proc. 23rd Intl Coastal Engng Conf., ASCE*, pp. 2758–2771.

https://doi.org/10.1017/S0022112098001694 Published online by Cambridge University Press